Characterization and Measurement of Performance Properties of the UFSOOK Camera Communication Protocol

Gyula Simon and Márk Rátosi

Abstract—Performance analysis of the undersampled frequency shift ON–OFF keying (UFSOOK) protocol, frequently used in visible light communication, is provided. Data transmission is modeled as a measurement process, and the analysis of the underlying measurement channel and the possible error sources reveals important performance properties of the protocol itself. The theoretical bit error rate, as a function of the receiver camera's sampling properties, the frequency error between the transmitter and the receiver, the measurement noise, and the parameters of the protocol, is derived. A measurement process is also proposed, with which the theoretical results are validated.

Index Terms—Camera communication, error analysis, protocol analysis, undersampled frequency shift ON–OFF keying (UFSOOK), visible light communication.

I. INTRODUCTION

LIGHTING fixtures utilizing light-emitting diodes (LEDs) became widespread in homes, offices, traffic, and industrial sites. Such LED lights allow the fast modulation of the light source, thus, in addition to their primary illumination purposes, LED lights can also be used as transmitters in visible light communication (VLC) systems. The widespread utilization of embedded cameras opened a special field of VLC, where on the receiver side a commercial camera (e.g., smartphone or industrial camera) is utilized. Due to the low frame rate of commercial cameras, such camera communication systems allow low communication bandwidth only but nevertheless offer a wide range of useful applications, e.g., transmitting traffic information or providing localization services [1].

For low-distance communication purposes, the rolling shutter effect was successfully utilized: the image of the blinking light source contains fringes, which can be used to decode the transmitted code [2]. A big advantage of this method is that a single image is enough for decoding.

For longer distances, where the captured image of the transmitter is small, such methods cannot be applied, rather various undersampled communication protocols have been proposed, where the fast-blinking transmitter is sampled with a relatively low frame-rate camera. Undersampled methods can decode the transmitted code using images containing a few pixels only (thus they can operate from long distances), but they require multiple consecutive images (a video stream). The coding scheme is designed so that the message can be decoded using the undersampled image sequence. In undersampled frequency shift ON–OFF Keying (UFSOOK), two different frequencies are used to code data, and a third frequency is utilized to denote the header. In this case, two symbols (hence two camera samples) are required to decode one bit [3] (see Section II for a detailed description). Undersampled phase shift ON–OFF keying uses one frequency only with different phase values to code data, providing faster transmission: one bit can be decoded using one symbol (plus some overhead due to the header and start frame delimiter) [4]. Undersampled pulse–amplitude modulation (PAM) combines phase and amplitude modulation to provide even higher bitrates, e.g., 64 bits/symbol, for short distances [5]. Undersampled pulsewidth modulation (PWM) replaces amplitude modulation with PWM, allowing simpler hardware solutions [6]. Recently compressed sensing methods have also been applied to design undersampled coding [7]. In order to provide higher bandwidth, parallel channels [8] and color coding [9] have also been proposed.

The basic performance characterization measure of digital communication channels is the bit error rate (BER), defined as the ratio of erroneous bit detections and the total number of transmitted bits [10]. The correct theoretical characterization of the channel requires good modeling of the underlying channel and the possible error sources, as it was emphasized in the case of various communication channels, e.g., power line communication systems [11], wireless industrial environments [12], or human-body communications [13].

The robustness and ease of implementation make the UFSOOK protocol attractive in real applications. In this article, we provide a novel comprehensive performance analysis of this protocol, by modeling the communication channel as a measurement process. It was shown in [14] that both the finite aperture time of the camera and the frequency offset between the unsynchronized camera and transmitter are potential error sources. As a new result, in this article, the findings of [14] will be extended: we will provide an enhanced combined

Gyula Simon is with the Alba Regia Technical Faculty, Óbuda University, 8000 Székesfehérvár, Hungary (e-mail: simon.gyula@amk.uni-obuda.hu).

Márk Rátosi is with the Department of Computer Science and Systems Technology, University of Pannonia, 8200 Veszprém, Hungary (e-mail: ratosi@dcs.uni-pannon.hu).
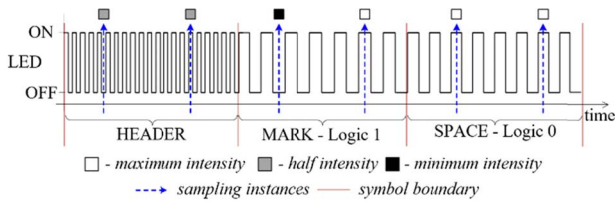
Fig. 1. Operation of UFSOOK protocol.

error model, and also the effect of measurement noise will be analyzed. As a result of the theoretical analysis, we will provide insight to protocol details, which allows the designer to tune protocol parameters to achieve the required performance by an educated compromise. The key findings are the following.

1) The minimal achievable BER of UFSOOK depends on the blinking frequency of the transmitter and the frequency offset between the transmitter and the camera.
2) There is an optimal range for the threshold parameter of the protocol around the middle point of the signal's intensity range, where the BER is minimal. The width of the optimal range is influenced by the camera aperture time.
3) In the case of nonideal threshold settings, the BER increases, depending on the threshold, the frequency offset, and the camera aperture time.
4) Typical amount of measurement noise has a minor effect around the ideal setting, but the BER may significantly be increased by the noise outside of the ideal parameter setting.

The theoretical findings were verified by real measurements. To allow controlled measurements of the performance properties, a special measurement method and a corresponding tool were developed.

Section II reviews the UFSOOK protocol. In Section III, the theoretical error analysis is presented. Section IV contains the description of the measurement method and the results of the measurements, which are compared to the theoretical findings.

II. OVERVIEW OF THE UFSOOK PROTOCOL

UFSOOK [3] is a simplex VLC protocol that can be used to transmit data between an ordinary camera as the receiver, and controllable LED beacons as the transmitters. The protocol's operation is illustrated in Fig. 1. For the transmission three different symbols are used: HEADER, MARK, and SPACE symbols, each symbol (or bit) requires two samples for decoding.

Data packets are preceded by a HEADER symbol (see Fig. 1). When data are continuously streamed, the HEADER symbol of the next packet can be used as a footer for the actual packet, thus framing can be achieved. MARK symbols represent the logical 1 values, containing two consecutive samples with different light intensities (i.e., ON–ON as in Fig. 1, or ON–OFF). SPACE symbols represent the logical 0 values, where two consecutive samples have the same light intensity (i.e., ON–ON as in Fig. 1, or OFF–OFF). Each symbol

is generated as a square wave with a different frequency, which can be chosen to seem flicker-free for the human eye, but not for the camera sensor. Thus, the communication protocol can be used in lighting infrastructures.

The HEADER symbol's time period is chosen to be small with respect to the sensor's exposure time (e.g., $f_{\text{HEADER}} > 10$ kHz), thus the camera senses it as a half (average) intensity light source, see the first two samples with detected half intensity signal values in Fig. 1. The SPACE symbol's frequency is chosen to be an integer multiple of the camera's sampling frequency:

$$f_{\text{SPACE}} = \frac{1}{T_{\text{SPACE}}} = nf_{\text{CAM}}. \tag{1}$$

This choice of frequency ensures that consecutive samples are taken at the same phase of the signal, thus providing the same values (see the last ON–ON sample pair in Fig. 1).

The MARK symbol's frequency is chosen as follows:

$$f_{\text{MARK}} = \frac{1}{T_{\text{MARK}}} = (n - 0.5) f_{\text{CAM}} \tag{2}$$

which leads to consecutive samples taken 180° out of phase, resulting in opposite signal values (see the second sample pair in Fig. 1, showing OFF–ON values).

As a typical example, a camera with a sampling rate of 30 Hz and $n = 4$ results $f_{\text{SPACE}} = 120$ Hz and $f_{\text{MARK}} = 105$ Hz. Notice that each symbol contains two samples, hence every symbol (i.e., bit) has a transmission time of $2/f_{\text{CAM}}$.

III. ERROR ANALYSIS

In this section, the main error sources of the UFSOOK protocol will be analyzed. First, the applied models for camera operation and the light sources will be introduced, followed by the analysis of the protocol. The effects of the frequency error between the camera and the transmitter are studied first, then we will analyze the effect of nonideal sampling.

A. Operation Model

In order to be able to perform mathematical analysis of the protocol's performance, a model on the operation of the camera and the light sources will be used.

The light source is assumed to be operating according to the UFSOOK protocol, i.e., it has constant frequency during the symbol transmission with a 50% duty cycle. (Note that the change of duty cycle (e.g., due to dimming) severely degrades the potential accuracy of the protocol, see [8]. In this article, we will consider the case of symmetrical signals only.) The signal shape is considered square: this assumption is valid for our investigation since the rise/fall times of LEDs and their driver circuits are orders of magnitude smaller than the smallest aperture times of commercial cameras.

We assume that the camera has a global shutter, i.e., the sampling of each pixel is performed simultaneously. The sampling is performed during the aperture time of the camera. If the aperture time is S and the luminous intensity of the
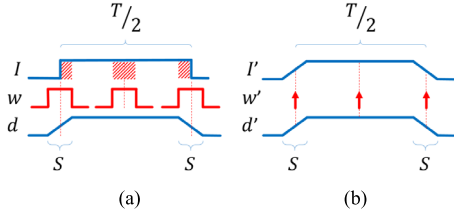
Fig. 2. Integral sampling and the equivalent model. (a) Integral sampling. I is the luminous intensity of the light source, w is the sampling window with aperture time S, and d is the detected light intensity as a function of the sampling time instant (which is at the center of the sampling window). (b) Equivalent model. $I' = d$ is the modified light source, w' is the impulse sampling, and $d' = d$ is the detected light intensity.

light source is $I(t)$, where t is the time, then the detected light intensity d at time instant t_0 is the following:

$$d(t_0) = \alpha \int_{t_0 - \frac{S}{2}}^{t_0 + \frac{S}{2}} I(t) \, dt + n(t_0) \tag{3}$$

where α depends on the camera's properties and settings (e.g., ISO number and aperture size) and n is the additive noise component. Notice that (3) is valid only when the camera is not saturated, i.e., the value computed in (3) is not larger than the maximum value the camera can represent (in cameras numbers are usually represented by 8–10-bit unsigned integers). The effect of saturation is out of the scope of this article, although the presented results can be expanded to model this phenomenon as well.

Fig. 2(a) illustrates the effect of sampling with an integral camera model. The square-wave light source's intensity signal I is sampled according to (3) in an aperture window w with width S The detected light intensity d as a function of the sampling time instant, has a trapezoidal shape, where the rising and falling edges have a width of S. Notice that the sampling time instant is the center of the aperture window, according to (3).

The operation of the system can be modeled with an equivalent model, illustrated in Fig. 2(b): the equivalent light source produces the trapezoidal intensity curve I' (instead of square wave I), as follows:

$$I'(t_0) = \int_{t_0 - S/2}^{t_0 + S/2} I(t) \, dt + n'(t_0) \tag{4}$$

while the camera performs pulse sampling [instead of the integral sampling of (3)]:

$$d'(t_0) = \alpha I'(t_0) \tag{5}$$

Since for $n(t_0) = \alpha n'(t_0)$ it is true that $d'(t_0) = d(t_0)$ for every time instant t_0, the two models are equivalent.

The camera is assumed to perform sampling with constant frequency (or frame rate) f_{CAM}. We assume that the short-term stability of the camera is good enough, so we can ignore the effects of frequency change or jitter.

We do not assume, however, that the light modulator and the camera are synchronized. This would be impractical in most applications, thus we allow slight differences between the ideal and real frequencies. Let the ideal camera frequency be f_{CAM}
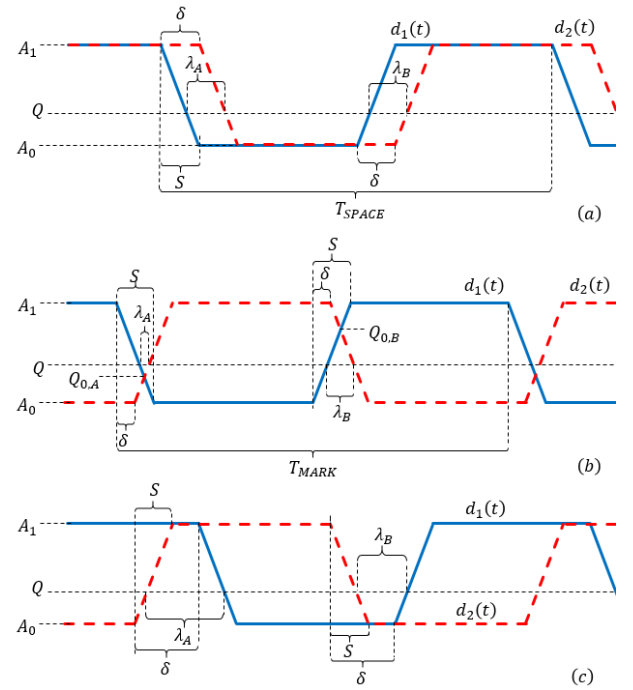

Fig. 3. Effect of frequency error on the sampling. (a) SPACE symbol, (b) MARK symbol with $\delta < S$, (c) MARK symbol with $\delta \geq S$.

and the corresponding ideal sampling period be $P = 1/f_{CAM}$, and let us assume that the modulator operates using this ideal frequency, according to (1) and (2). If the actual camera frequency is $\tilde{f}_{CAM} = 1/\tilde{P}$ then let us denote the difference between the ideal and actual sampling interval by δ, as follows:

$$\delta = \frac{1}{\tilde{f}_{CAM}} - \frac{1}{f_{CAM}} = \tilde{P} - P. \tag{6}$$

B. Frequency Offset

Let us define the noise-free samples $d_1(t)$ and $d_2(t)$ as follows:

$$\begin{aligned} d_1(t) &= \alpha I'(t) \\ d_2(t) &= \alpha I'\left(t + \tilde{P}\right) \end{aligned} \tag{7}$$

where $d_1(t)$ represents a potential first sample of a symbol, in case the sampling occurs at time t (called primary sampling time), while the next sample, sampled $\tilde{P}$ time later, will be denoted by $d_2(t)$. The decoding graphs, shown in Fig. 3, contain $d_1(t)$ (solid blue lines) and $d_2(t)$ (dashed red lines). Thus, from the decoding graphs, for each symbol, the value of the first and the corresponding second sample can be read, as a function of the primary sampling time.

In the case of the SPACE symbol, according to (1), $I(t) = I(t + P)$, thus also $I'(t) = I'(t + P)$. If δ error is present according to (4) then $I'(t) = I'(t + \tilde{P} - \delta)$, thus $d_1(t) = d_2(t - \delta)$; in this case, the two curves of the decoding graph are shifted by δ, as shown in Fig. 3(a). For the MARK symbol, however, $I(t) = !I(t + P)$, according to (2), where $!$ denotes the opposite intensity value. If $I(t)$ varies between I_0 and I_1 then $I(t)$ can be expressed as $I(t) = I_0 + I_1 - I(t+P)$.

Similarly, if $I'(t) = d(t)$ varies between A_0 and A_1 then $I'(t) = A_0 + A_1 - I'(t + P)$ thus $d_1(t) = A_0 + A_1 - d_2(t - \delta)$. Thus, the decoding graph for the MARK symbol contains a trapezoid signal and its shifted inverse, as shown in Fig. 3(b) and (c), for different values of δ.

The decoding graph also contains the threshold Q. If $d(t) > Q$ then the detected source is considered to be ON, otherwise, it is OFF. Ideally, for SPACE symbols either $d_1(t) > Q$ and $d_2(t) > Q$ (ON–ON) or $d_1(t) \leq Q$ and $d_2(t) \leq Q$ (OFF–OFF); and for MARK symbols the samples are either $d_1(t) > Q$ and $d_2(t) \leq Q$ (ON–OFF) or $d_1(t) \leq Q$ and $d_2(t) > Q$ (OFF–ON). However, as Fig. 3 shows, there are time intervals, the lengths of which are denoted by λ_A and λ_B, where these constraints do not hold and thus the symbol decoding returns false results. Let us call these intervals "dangerous."

In the synchronized case (when the frequency error is $\delta = 0$), the sampling is always performed at the same phase of the blinking signal, thus the decoding is either always good (the primary sampling time is not in a dangerous interval), or it is always bad (the primary sampling time is inside of a dangerous interval). In the unsynchronized case ($\delta \neq 0$), however, the phase of the sampling time is continuously changing, thus the primary sampling time sweeps along the timeline. The detection is good, while the primary sampling time is outside of the dangerous intervals; and the detection is faulty, when the primary sampling time is inside of one of the dangerous intervals.

First, let us investigate the detection graph for SPACE symbols. As Fig. 3(a) clearly shows, the width of the dangerous intervals is $\lambda_A = \lambda_B = \delta$ Since there are two dangerous intervals with a cumulative length of 2δ in a blinking period T_{SPACE}, the BER μ_{SPACE} in the case of $\delta \neq 0$ can be estimated as follows:

$$\mu_{\text{SPACE}} = \frac{2\delta}{T_{\text{SPACE}}} = 2\delta n f_{\text{CAM}}. \tag{8}$$

Now let us examine the MARK symbol. Here the two cases of $\delta < S$ and $\delta \geq S$ will be separately handled. The case of $\delta < S$ is shown in Fig. 3(b). The signal amplitudes at the intersections of $d_1(t)$ and $d_2(t)$ are denoted by $Q_{0,A}$ and $Q_{0,B}$, as shown in Fig. 3(b). Using similar triangles it follows that

$$\frac{Q_{0,A} - A_0}{\frac{S-\delta}{2}} = \frac{A_1 - A_0}{S} \tag{9}$$

$$\frac{A_1 - Q_{0,B}}{\frac{S-\delta}{2}} = \frac{A_1 - A_0}{S} \tag{10}$$

from which the values of $Q_{0,A}$ and $Q_{0,B}$ can be expressed as

$$Q_{0,A} = \frac{A_1 + A_0}{2} - \frac{A_1 - A_0}{2} \frac{\delta}{S} \tag{11}$$

$$Q_{0,B} = \frac{A_1 + A_0}{2} + \frac{A_1 - A_0}{2} \frac{\delta}{S}. \tag{12}$$

If $Q_{0,A} \leq Q \leq Q_{0,B}$ (as the illustration of Fig. 3(b) shows) then λ_A and λ_B can be calculated, using similar triangles, as follows:

$$\frac{Q - Q_{0,A}}{\lambda_A} = \frac{A_1 - A_0}{2S} \tag{13}$$

$$\frac{Q_{0,B} - Q}{\lambda_B} = \frac{A_1 - A_0}{2S} \tag{14}$$

from which

$$\lambda_A = (Q - Q_{0,A}) \frac{2S}{A_1 - A_0} \tag{15}$$

$$\lambda_B = (Q_{0,B} - Q) \frac{2S}{A_1 - A_0}. \tag{16}$$

Using (11)–(12) and (15)–(16), it follows that

$$\lambda_A + \lambda_B = 2\delta. \tag{17}$$

Now let us consider the case of $Q < Q_{0,A}$ [not shown in Fig. 3(b)]. Again, using similar triangles, the following results can be obtained:

$$\lambda_A = (Q_{0,A} - Q) \frac{2S}{A_1 - A_0} \tag{18}$$

$$\lambda_B = (Q_{0,B} - Q) \frac{2S}{A_1 - A_0} \tag{19}$$

from which it follows that

$$\lambda_A + \lambda_B = \frac{2S}{A_1 - A_0} (Q_{0,A} + Q_{0,B} - 2Q). \tag{20}$$

Using (11) and (12), it follows that

$$\lambda_A + \lambda_B = \frac{2S}{A_1 - A_0} (A_1 + A_0 - 2Q). \tag{21}$$

Similarly, for the case of $Q > Q_{0,B}$, the following results can be obtained:

$$\lambda_A + \lambda_B = \frac{2S}{A_1 - A_0} (2Q - (A_1 + A_0)). \tag{22}$$

The results (17), (21), and (22) for the MARK symbol can be summarized as follows:

$$\lambda_A + \lambda_B = \begin{cases} 2\delta, & \text{if } Q_{0,A} \leq Q \leq Q_{0,B} \\ \dfrac{2S}{A_1 - A_0} |A_1 + A_0 - 2Q|, & \text{otherwise.} \end{cases} \tag{23}$$

Thus, the BER estimate for MARK symbol, for the case of $\delta < S$, is the following:

$$\mu_{\text{MARK}} = \begin{cases} 2\delta/T_{\text{MARK}}, & \text{if } Q_{0,A} \leq Q \leq Q_{0,B} \\ \dfrac{2S}{T_{\text{MARK}}} \dfrac{|A_1 + A_0 - 2Q|}{A_1 - A_0}, & \text{otherwise.} \end{cases} \tag{24}$$

The case $\delta \geq S$ is illustrated in Fig. 3(c). For this case, with geometrical calculations, similar to the previous cases, λ_A and λ_B can be derived as follows:

$$\lambda_A = \delta + S \frac{A_0 + A_1 - 2Q}{A_1 - A_0} \tag{25}$$

$$\lambda_B = \delta - S \frac{A_0 + A_1 - 2Q}{A_1 - A_0}. \tag{26}$$

Thus, for the case of $\delta \geq S$, the BER is the following:

$$\mu_{\text{MARK}} = \frac{\lambda_A + \lambda_B}{T_{\text{MARK}}} = \frac{2\delta}{T_{\text{MARK}}} = 2\delta (n - 0.5) f_{\text{CAM}}. \tag{27}$$

$$Q_{0,A} = Q_0 - \frac{\delta}{S}\frac{A_1 - A_0}{2} \qquad Q_0 = \frac{A_0 + A_1}{2} \qquad Q_{0,B} = Q_0 + \frac{\delta}{S}\frac{A_1 - A_0}{2}$$
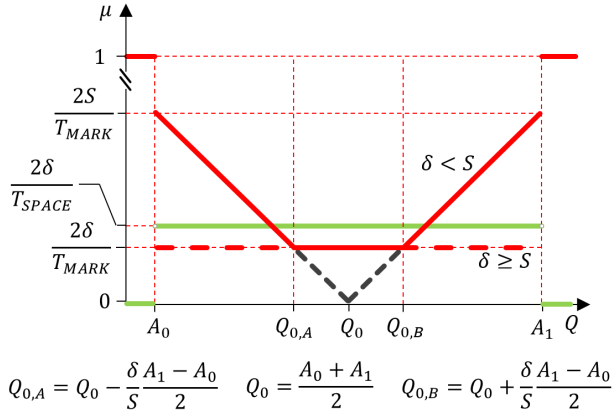
Fig. 4. BER, as a function of threshold Q. Green: SPACE symbols, solid red: MARK symbols with $\delta < S$, dashed red: MARK symbols with $\delta \geq S$.

The BER, as a function of threshold parameter Q according to (8), (24), and (27), is shown in Fig. 4. For extreme choices of Q, i.e., $Q < A_0$ or $Q \geq A_1$ everything is detected as SPACE, thus for $\mu_{\text{MARK}} = 100\%$ and $\mu_{\text{SPACE}} = 0$. For values of Q between the minimum and maximum detected light intensity, the value of BER μ_{SPACE} depends on δ, n, and f_{CAM} but does not depend on Q, according to (8). Similarly, if $\delta \geq S$, μ_{MARK} does not depend on Q, according to (27). When $\delta < S$, for threshold values between $Q_{0,A}$ and $Q_{0,B}$ the BER for MARK symbols is minimal, with a value of $2\delta / T_{\text{MARK}}$, which is identical to (27). For $Q < Q_{0,A}$ or $Q > Q_{0,B}$ the BER value increases as Q approaches the minimum or maximum light intensity:

$$\mu_{\text{MARK}}(A_0) = \mu_{\text{MARK}}(A_1) = \frac{2S}{T_{\text{MARK}}}. \qquad (28)$$

The results show that the BER is proportional with the δ time difference between ideal and real camera sampling interval, the n design parameter, and the f_{CAM} camera frame rate. In practice, n must be high enough to provide flicker-free operation (i.e., $nf_{\text{CAM}} \gg 100$ Hz), but our results also suggest that n should be chosen as small as possible (while satisfying the flicker-free requirements), in order to provide small BER.

The results also indicate that the detection quality for SPACE symbol does not depend on the threshold parameter Q, while for the optimal detection of MARK symbols Q should be chosen between Q_A and Q_B (thus the mean of the signal is a good choice). If this cannot be guaranteed, the BER is proportional with the aperture time S and inversely proportional with the signal's amplitude $A_1 - A_0$, thus S should be kept small (preferably below δ, when the BER does not depend on the exact value of Q), and low signal amplitudes should be avoided. Thus, the following design rules can be stated in order to provide low BER.

1) The frequency offset should be kept small since the minimum error depends on this value.
2) The threshold should be close to the ideal value of $Q_0 = (A_0 + A_1)/2$
3) Small aperture time should be used to minimize the effect of suboptimal threshold.

4) Design parameter n should be small to provide large T_{SPACE} and T_{MARK} (while satisfying the requirements of flicker-free operation) to provide small minimum value for the error.
5) The signal amplitude should be as high as possible to provide a wide range for optimal threshold and also to provide high signal-to-noise ratio (see Section III-C).

C. Effect of Noise

For the noise analysis, we assume that the measurement noise can be modeled as additive white Gaussian noise (AWGN). Thus, the noisy detection signals are

$$\check{d}_1(t) = d_1(t) + n_1(t) \qquad (29)$$
$$\check{d}_2(t) = d_2(t) + n_2(t) \qquad (30)$$

where $d_1(t)$ and $d_2(t)$ are the noise-free samples, and $n_1(t)$ and $n_2(t)$ are the AWGN components with distribution $N(0, \sigma^2)$.

For SPACE symbols, detection error occurs when the detected light intensities are the same, i.e., in the following two cases:

(a) $\check{d}_1(t) > Q$ and $\check{d}_2(t) > Q$ or
(b) $\check{d}_1(t) \leq Q$ and $\check{d}_2(t) \leq Q$.

Let the Q-function $Qf(x)$ denote the probability that random variable X with distribution $N(0, \sigma^2)$ is higher than x:

$$Qf(x) = P(X > x) = \frac{1}{2} - \frac{1}{2}\text{erf}\left(\frac{x}{\sigma\sqrt{2}}\right). \qquad (31)$$

If the threshold is Q then the probability that the detection, with primary sampling time t, is false due to case (a) is the following:

$$P_{\text{err}-a}(t, Q) = Qf_1(t, Q)\, Qf_2(t, Q) \qquad (32)$$

where $Qf_1(t, Q) = Qf(Q - d_1(t))$ and $Qf_2(t, Q) = Qf(Q - d_2(t))$. Similarly, the probability of false detection due to case (b) is the following:

$$P_{\text{err}-b}(t, Q) = (1 - Qf_1(t, Q))(1 - Qf_2(t, Q)). \qquad (33)$$

For MARK symbols, erroneous detection can happen when the detected light intensities are different, in the following two cases:

(c) $\check{d}_1(t) > Q$ and $\check{d}_2(t) \leq Q$ or
(d) $\check{d}_1(t) \leq Q$ and $\check{d}_2(t) > Q$.

Given the threshold value Q the probabilities of false detections, due to case (c) and (d), are the following:

$$P_{\text{err}-c}(t, Q) = Qf_1(t, Q)(1 - Qf_2(t, Q)) \qquad (34)$$
$$P_{\text{err}-d}(t, Q) = (1 - Qf_1(t, Q))\, Qf_2(t, Q). \qquad (35)$$

Using (32) and (33), the probability of false detections $P_{\text{err}}(t, Q)$ for SPACE symbols can be computed as follows:

$$P_{\text{err,SPACE}}(t, Q) = P_{\text{err}-a} + P_{\text{err}-b}. \qquad (36)$$

Similarly, using (34) and (35), for MARK symbols, the probability of false detections is the following:

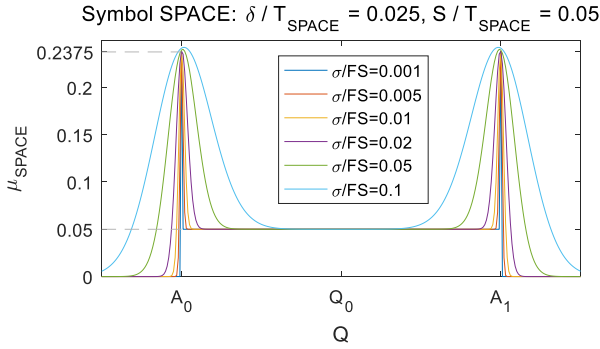$$P_{\text{err,MARK}}(t, Q) = P_{\text{err}-c} + P_{\text{err}-d}. \qquad (37)$$

Fig. 5. BER for SPACE symbols, as a function of threshold Q, in the presence of additive noise with variance σ.
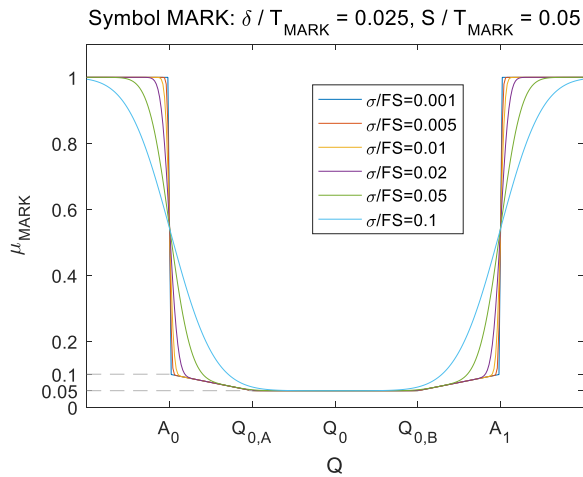

Fig. 6. BER for MARK symbols, as a function of threshold Q, in the presence of additive noise with variance σ.

The BER can be estimated as follows:

$$\mu = \frac{1}{T}\int_0^T P_{\mathrm{err}}(t, Q)\, dt \cong \frac{1}{K}\sum_{k=1}^K P_{\mathrm{err}}\left(k\frac{T}{K}, Q\right) \quad (38)$$

where $T = T_{\mathrm{SPACE}}$ and $P_{\mathrm{err}} = P_{\mathrm{err,SPACE}}$ for SPACE symbols and $T = T_{\mathrm{MARK}}$ and $P_{\mathrm{err}} = P_{\mathrm{err,MARK}}$ for MARK symbols. The rightmost expression of (38) is a practical discrete approximation using K sample points.

The BER, as a function of Q, is illustrated in Figs. 5 and 6, where the BER was calculated using the discrete approximation of (38), for $\delta/T = 0.025$, $S/T = 0.05$, and FS $= A_1 - A_0 = 20$. The figures show various signal-to-noise levels: the ratio of $\sigma/$FS varied from 0.001 to 0.1. The shape of the BER function for SPACE symbols, shown in Fig. 5, for small values of Q converges to the noise-free case, shown by green in Fig. 4: for Q between A_0 and A_1, according to (8), $\mu_{\mathrm{SPACE}} = 2\delta/T_{\mathrm{SPACE}} = 0.05$, while outside of this region $\mu_{\mathrm{SPACE}} = 0$, which corresponds to the calculated shape of Fig. 5. Notice that for noiseless case the BER function has a rectangular shape, but in the presence of noise, two pulses appear around A_0 and A_1, of which the width depends on the noise level (wider pulse for higher noise). The amplitude of the pulse can be derived as follows. Let the threshold be A_0 and the noise variance be higher than 0. When either of

the detected samples is low [i.e., $d_1 \cong A_0$ or $d_2 \cong A_0$, see Fig. 3(a)] then the probability of the false detection is 50%, for arbitrarily small, positive noise variances. For higher values of d_1 and d_2 the probability of false detections is close to 0 for small noise levels. Since the total time of either d_1 or d_2 being close to A_0 is $T_{\mathrm{SPACE}}/2 - S + \delta$, the BER at A_0 in the presence of noise is

$$\mu_{\mathrm{SPACE}}(A_0) = 0.5\frac{\frac{T_{\mathrm{SPACE}}}{2} - S + \delta}{T_{\mathrm{SPACE}}} = 0.25 + \frac{\delta - S}{2T_{\mathrm{SPACE}}}. \quad (39)$$

The same argument can be repeated for threshold A_1, thus

$$\mu_{\mathrm{SPACE}}(A_1) = 0.25 + \frac{\delta - S}{2T_{\mathrm{SPACE}}}. \quad (40)$$

In the case shown in Fig. 5, the value of the BER at A_0 and A_1, according to (39)–(40), is $0.25 - 0.0125 = 0.2375$, which corresponds well to the values shown in Fig. 5. Notice that the effect of noise is especially significant around the smallest and highest detected light intensities A_0 and A_1. Around the optimal choice of $Q_0 = (A_0 + A_1)/2$, however, the effect of noise is hardly observable.

Fig. 6 shows the BER functions for MARK symbols. For small noise levels, the shape of μ_{MARK} is similar to the function shown in Fig. 4 with a solid red line. According to (11) and (12), $Q_0 - Q_{0,A} = Q_{0,B} - Q_0 = \mathrm{FS}\cdot\delta/2S = \mathrm{FS}/4$; and according to (24), the minimum of the function, around the optimal value, is $2\delta/T_{\mathrm{MARK}} = 0.05$, while $\mu_{\mathrm{MARK}}(A_0) = \mu_{\mathrm{MARK}}(A_1) = 2S/T_{\mathrm{MARK}} = 0.1$, and the BER is 100% below A_0 and above A_1: these theoretical results are accurately represented by the function shown by the deep blue line in Fig. 6. For higher noise levels, the function gets distorted, especially around A_0 and A_1. Notice again that the effect of noise is small for threshold values close to the optimum.

The theoretical results will be verified by real measurements in Section IV.

IV. MEASUREMENTS

The purpose of the measurements is to validate the theoretical BER results derived in Section III. Thus, the two data symbols, SPACE and MARK, were separately tested in a well-controlled environment. First, the measurement setup and the devices used in the measurement will be introduced, and then the measurement results will be presented and evaluated.

A. Measurement Setup

The measurement setup is illustrated in Fig. 7. The modulated signal was generated by a microcontroller unit (MCU) through a MOSFET LED driver. The LEDs were placed in separate closed (black) optical measurement chambers, in order to exclude external disturbances. In the experiment, two separate channels were used to test the behavior of the protocol's MARK and SPACE symbols: Channel 1 was dedicated to MARK symbols, while in Channel 2 SPACE symbols were transmitted. Notice that the purpose of the test was to determine the error sensitivity of the data symbols, thus only the symbols were transmitted continuously without any data framing (i.e., no HEADER was used). Each symbol's
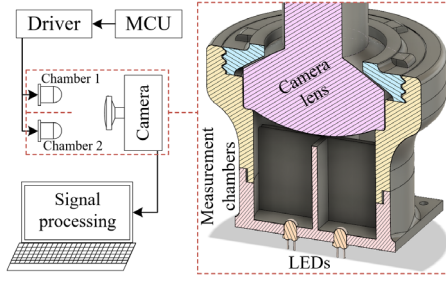
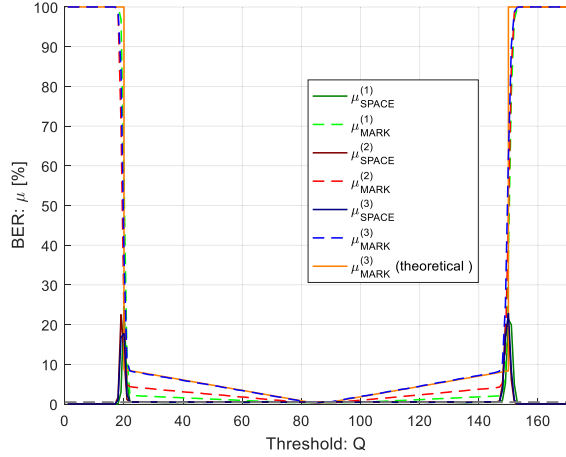Fig. 7. Measurement setup: hardware components (left-hand side) and the optical measurement chambers.

Fig. 8. Measured BER values for constant δ and three different values of S, as a function of Q.

Fig. 9. Measured BER values for constant δ and three different values of S, as a function of Q (zoomed). The theoretical BER diagram for MARK symbols in experiment 3 is also shown.

Fig. 10. Measured BER for constant S and various values of δ, as a function of Q.

channel was simultaneously observed by the same camera. The recorded video stream was processed offline with optional controlled additive noise.

The nominal frame rate of the camera was 30 frames/s. The design parameter n was set to 4, thus the frequencies of the SPACE and MARK symbols were ideally 120 and 105 Hz, respectively. Since the exact camera sampling rate slightly differs from the nominal value, and we wanted to experiment with multiple slip values, we fine-tuned the LED frequencies to provide the required amount of slip. In the experiments, we set slip values between 20 and 180 μs [14]. The detected signal range was between $A_0 \cong 20$ and $A_1 \cong 150$ with the 8-bit camera. The exposure time of the camera was varied between $S = 100$ μs and $S = 400$ μs.

B. Measurement Results

Each symbol channel was processed separately, and the numbers of good and bad detections were determined, as a function of threshold parameter Q. The calculated symbol error rates are presented in the following figures.

Figs. 8 and 9 show the BER results of three experiments with $S^{(1)} = 100$ μs, $S^{(2)} = 200$ μs, and $S^{(3)} = 400$ μs when $\delta = 20$ μs was constant. The noise variance was below 1 bit. The light intensities of the LEDs were set so that the minimum and maximum detected amplitudes were approximately the same in each experiment. The representative values $Q_{A,0}$, Q_0, $2\delta/T_{MARK}$, $2\delta/T_{SPACE}$, and $2S^{(i)}/T_{MARK}$ are also shown in the figures (compare with Fig. 4). For easier comparison,
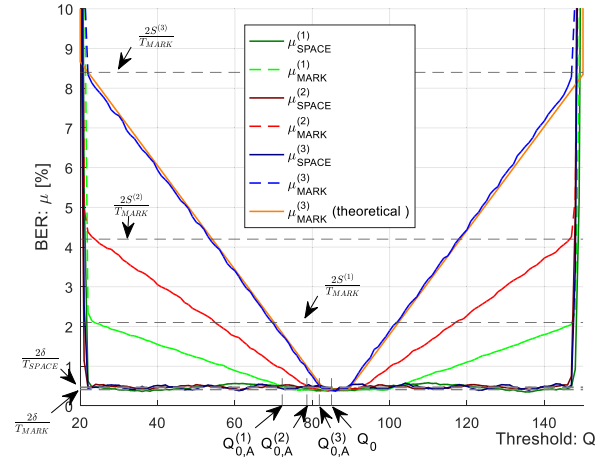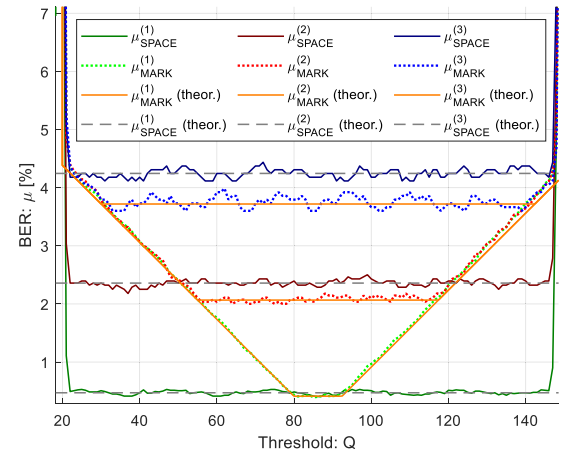
a theoretical BER diagram for MARK symbols is also shown (for better visibility, only for experiment 3). The measurements fit the theoretical results with remarkable accuracy.

The effect of frequency inaccuracies is illustrated in Fig. 10. In the experiments, constant aperture time of $S = 200 \mu$s was used, and the camera frequency was $f_{CAM} = 30.027$ Hz. For this camera, the ideal symbol sequences are $f_{MARK} = 105.096$ Hz and $f_{SPACE} = 120.110$ Hz. In the measurements, three different cases were examined with $f_{MARK,1} = 105.159$ Hz and $f_{SPACE,1} = 120.181$ Hz $f_{MARK,2} = 105.408$ Hz and $f_{SPACE,2} = 120.467$ Hz and $f_{MARK,3} = 105.659$ Hz and $f_{SPACE,3} = 120.753$ Hz. These symbol frequencies result slip values of $\delta_1 = 20$ μs, $\delta_2 = 98$ μs, and $\delta_3 = 177$ μs. Fig. 10 contains the measurement results as well as the theoretical BER functions: orange and gray curves correspond to MARK and SPACE symbols, respectively. The measured minimal achievable BER is directly proportional to the slip for both the SPACE and MARK symbols corresponding to (8) and (24), respectively. As the figure clearly shows that the measurement results fit the theoretical results.

The effect of noise is shown in Fig. 11 for $S = 200$ μs and $\delta = 98$ μs. The variance of the additive noise component was
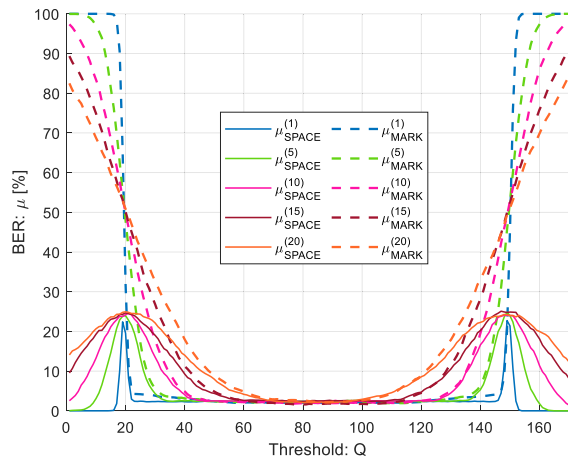
Fig. 11.   Measured and theoretical symbol error rates (zoomed).

set to 1, 5, 10, 15, and 20 LSB (notice that the camera was used in 8-bit mode). Comparing with Figs. 5 and 6, the measured BER functions correspond well with the theoretical results.

The presented measurements are in good agreement with the theoretical results. Thus, the derived theoretical model can be used to design the parameters of the protocol and also to predict the performance of the protocol.

V. Conclusion

The performance of the UFSOOK protocol was analyzed. The decoder was modeled as a measurement process, including the camera's nonideal (integral) sampling, the frequency slip between the camera and the light source, and the measurement noise.

The results show that the frequency slip causes detection errors for both the SPACE and MARK symbols, the smallest possible BER being proportional to the slip. The best BER can be achieved by the optimal choice of the protocol's threshold parameter around the mean value of the minimum and maximum detected signal levels. The width of the possible range for optimal values depends on the camera's aperture time.

For nonideal settings, the BER increases as a function of the threshold parameter and the aperture time for MARK symbols only. The measurement noise significantly increases the BER if the threshold parameter is close to the minimum or maximum detected signal levels, but the noise effect is small when the threshold is close to the optimum.

The BER is proportional to the blinking frequency, thus it should be kept as small as possible. Since in most applications flickering must be avoided, as a compromise, the blinking frequency should be set to the minimal frequency value where the flickering effect is not perceptible.

The theoretical results were validated by real physical measurements. A special measurement setup was used to separately study the BERs of both data symbols, as a function of design parameters, physical (camera) parameters, and the unwanted external disturbances. The measurements provided a very good agreement with the theoretical results.

References

[1] G. Simon, G. Zachar, and G. Vakulya, "Lookup: Robust and accurate indoor localization using visible light communication," *IEEE Trans. Instrum. Meas.*, vol. 66, no. 9, pp. 2337–2348, Sep. 2017.

[2] C. Danakis, M. Afgani, G. Povey, I. Underwood, and H. Haas, "Using a CMOS camera sensor for visible light communication," in *Proc. IEEE Globecom Workshops*, Anaheim, CA, USA, Dec. 2012, pp. 1244–1248.

[3] R. D. Roberts, "Undersampled frequency shift ON-OFF keying (UFSOOK) for camera communications (CamCom)," in *Proc. 22nd Wireless Opt. Commun. Conf.*, Chongqing, China, May 2013, pp. 645–648.

[4] P. Luo, Z. Ghassemlooy, H. Le Minh, X. Tang, and H.-M. Tsai, "Undersampled phase shift ON-OFF keying for camera communication," in *Proc. 6th Int. Conf. Wireless Commun. Signal Process. (WCSP)*, Hefei, China, Oct. 2014, pp. 1–6.

[5] P. Luo, Z. Ghassemlooy, H. L. Minh, H.-M. Tsai, and X. Tang, "Undersampled-PAM with subcarrier modulation for camera communications," in *Proc. Opto-Electron. Commun. Conf. (OECC)*, Shanghai, China, Jun. 2015, pp. 1–3.

[6] P. Luo, T. Jiang, P. A. Haigh, Z. Ghassemlooy, and S. Zvanovec, "Undersampled pulse width modulation for optical camera communications," in *Proc. IEEE Int. Conf. Commun. Workshops (ICC Workshops)*, Kansas City, MO, USA, May 2018, pp. 1–6.

[7] B. W. Kim and S.-Y. Jung, "Novel flicker-free optical camera communications based on compressed sensing," *IEEE Commun. Lett.*, vol. 20, no. 6, pp. 1104–1107, Jun. 2016.

[8] R. D. Roberts, "A MIMO protocol for camera communications (CamCom) using undersampled frequency shift ON-OFF keying (UFSOOK)," in *Proc. IEEE Globecom Workshops (GC Wkshps)*, Atlanta, GA, USA, Dec. 2013, pp. 1052–1057.

[9] P. Luo *et al.*, "Experimental demonstration of RGB LED-based optical camera communications," *IEEE Photon. J.*, vol. 7, no. 5, Oct. 2015, Art. no. 7904212.

[10] S. M. Berber, "An automated method for BER characteristics measurement," *IEEE Trans. Instrum. Meas.*, vol. 53, no. 2, pp. 575–580, Apr. 2004.

[11] A. Cataliotti, V. Cosentino, D. Di Cara, and G. Tine, "Measurement issues for the characterization of medium voltage grids communications," *IEEE Trans. Instrum. Meas.*, vol. 62, no. 8, pp. 2185–2196, Aug. 2013.

[12] F. Barac, M. Gidlund, and T. Zhang, "Scrutinizing bit- and symbol-errors of IEEE 802.15.4 communication in industrial environments," *IEEE Trans. Instrum. Meas.*, vol. 63, no. 7, pp. 1783–1794, Jul. 2014.

[13] M. D. Pereira, G. A. Alvarez-Botero, and F. Rangel de Sousa, "Characterization and modeling of the capacitive HBC channel," *IEEE Trans. Instrum. Meas.*, vol. 64, no. 10, pp. 2626–2635, Oct. 2015.

[14] M. Ratosi and G. Simon, "Performance analysis of the UFSOOK protocol," in *Proc. IEEE Int. Symp. Meas. Netw. (M&N)*, Catania, Italy, Jul. 2019, pp. 1–6.

Gyula Simon received the M.Sc. and Ph.D. degrees in electrical engineering from the Budapest University of Technology, Budapest, Hungary, in 1991 and 1998, respectively.

He is currently a Professor with the Alba Regia Technical Faculty, Óbuda University, Székesfehérvár, Hungary. His research interests include adaptive signal processing, localization, and sensor networks.

Márk Rátosi received the M.Sc. degree in engineering information technology from the University of Pannonia, Veszprém, Hungary, in 2018, where he is currently pursuing his Ph.D.

His main research interests include embedded systems and localization.